Phase Field Modeling of Fracture and Composite Materials

Robert Spatschek, Denis Pilipenko, Clemens Müller-Gugenberger, and Efim A. Brener
Institut für Festkörperforschung, Forschungszentrum Jülich, D-52425 Jülich, Germany

September 28, 2006

Abstract

The phase field method is a very powerful numerical method to solve moving boundary problems. Here we demonstrate how it can be applied to various processes involving sound propagation and fracture. This approach is related to a new theory of fracture which describes in particular the fast growth of cracks. We study the propagation of elastic waves, the determination of stress intensity factors for moving cracks with extended tips, and the interaction and coarsening of cracks. Other examples are the influence of elastic effects on phase transitions and the delamination in composite materials.

Keywords: Fracture Mechanics, Phase Field Methods, Sound propagation, Composite materials

1 Introduction

Understanding the phenomenon of fracture, especially in composite materials, is very important for many industrial applications. Apart from the development of physically motivated and suitable models for crack propagation [1], numerical tools are needed to describe the elastic deformations in complex materials. Then, for example, the acoustic properties of a composite structure can be used for nondestructive testing.

The aim of this article is to demonstrate the capabilities of the phase field method for these processes. It can be used not only to study the wave propagation in materials consisting of several different materials or phases, but also to study the crack propagation in homogeneous or composite materials. This method is numerically very robust and able to describe even difficult topological changes due to phase transitions or merging of cracks.

The general idea of the phase field method is not to track the location of interfaces or defects explicitly, but instead to introduce a so called phase field. In the simplest case of a two-phase material, which can consist for example of a hard and a soft solid phase, the value $\phi = 1$ is assigned to the hard and $\phi = 0$ to the soft phase. If the transition between the phases is now smoothed out on a small numerical length scale ξ (instead of a sharp transition from $\phi = 0$ to $\phi = 1$), the motion of interfaces can be mapped to a partial differential equation for the phase field on the entire domain. In particular, the boundary conditions at interfaces are automatically satisfied.

The paper is organized as follows: First, in section 2 we introduce a phase field model which can be used to study elastically induced phase transitions and fracture processes. In sections 3 and 4 we give two basic applications, the propagation of waves in composite materials and the determination of stress intensity factors. Here, the phase field dynamics is not relevant and only the elastic properties are investigated. Starting from section 5, the phase field dynamics is discussed e.g. for the interplay of many growing cracks or elastically induced phase transitions. A more complicated multiphase application is the delamination of two elastic media, as described in section 7. Here, also aspects of nondestructive testing are investigated.

2 Phase field modeling

For simplicity we assume a two-dimensional plane strain situation, linear elastic isotropic media and the mass density ρ to be equal in both phases. Let ϕ denote the phase field with values $\phi = 0$ for a "soft" phase inside a crack and $\phi = 1$ for a "hard" phase. We start the description from an energy functional, which consists of the following contributions: The elastic energy density is $f_{el} = \mu(\phi)\epsilon_{ij}^2 + \lambda(\phi)(\epsilon_{ii})^2/2$, with $\mu(\phi) = h(\phi)\mu^{(1)} + (1-h(\phi))\mu^{(2)}$ and $\lambda(\phi) = h(\phi)\lambda^{(1)} + (1-h(\phi))\lambda^{(2)}$, where $h(\phi) = \phi^2(3-2\phi)$ interpolates between the phases and the superscripts denote the bulk values; ϵ_{ik} and σ_{ik} are strain and stress tensor respectively, which are connected by Hooke's law for isotropic elasticity, $\sigma_{kj} = 2\mu\epsilon_{kj} + \lambda\epsilon_{ll}\delta_{kj}$, with the Lamé coefficient λ and the shear modulus μ. Alternatively, we use Young's modulus $E = \mu(3\lambda+2\mu)/(\lambda+\mu)$ and the Poisson ratio $\nu = \lambda/2(\lambda+\mu)$ as elastic constants.

The surface energy is $f_s(\phi) = 3\gamma\xi(\nabla\phi)^2/2$ with the interface width ξ and the surface energy density γ. Finally, $f_{dw} = 6\gamma\phi^2(1-\phi)^2/\xi$ is a double well potential. Thus the total potential energy is

$$U = \int dV \left(f_{el} + f_s + f_{dw}\right). \tag{1}$$

The elastodynamic equations are derived from the energy by the variation with respect to the displacements u_i,

$$\rho\ddot{u}_i = -\frac{\delta U}{\delta u_i}, \tag{2}$$

and the dissipative phase fields dynamics follows from

$$\frac{\partial\phi}{\partial t} = -\frac{D}{3\gamma\xi}\frac{\delta U}{\delta\phi} \tag{3}$$

with a kinetic coefficient D with dimension $[D] = \mathrm{m}^2\mathrm{s}^{-1}$.

From these equations, the following sharp interface limit ($\xi \to 0$) can be extracted [2]: With the premise of coherency at the interface and vanishing elastic constants in the soft phase, the solid matrix is free of normal and shear stresses at a crack contour, i.e. $\sigma_{nn} = \sigma_{n\tau} = 0$, which serves as boundary conditions (n and τ denote the normal and tangential directions at an interface). In the bulk, the elastic displacements u_i have to fulfill Newton's equation of motion,

$$\frac{\partial\sigma_{ij}}{\partial x_j} = \rho\ddot{u}_i. \tag{4}$$

The motion of the interface is locally expressed by the normal velocity

$$v_n = \frac{D}{\gamma\Omega}\Delta\mu \tag{5}$$

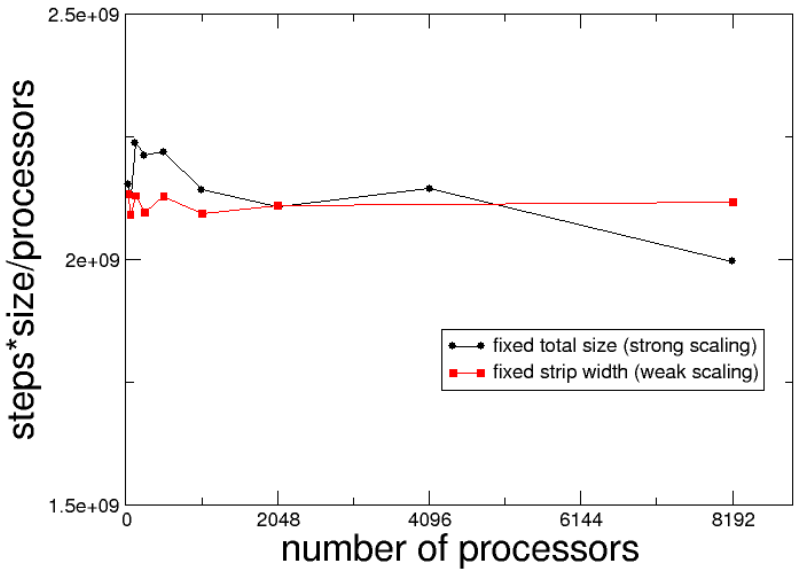

Figure 1: Scaling behavior of the parallelized phase-field code. An ideal speedup would correspond to a constant horizontal line. One can see that the parallelization is extremely efficient.

with the same kinetic coefficient D as above, and Ω denotes the atomic volume. Here, the difference in the chemical potentials between two phases at an interface is [3]

$$\Delta\mu = \Omega\left(\frac{1}{2}\sigma_{jk}\epsilon_{jk} - \gamma\kappa\right). \tag{6}$$

The interface curvature κ is positive if the crack shape is convex.

For the numerical realization, we employ explicit representations of both the elastodynamic equations and the phase field dynamics, where the elastic displacements are defined on a staggered grid [4]. We then choose a rectangular strip with fixed displacements at its upper and lower boundary to study crack growth. In the soft phase, we typically set the elastic constants to one millionth of the values in the hard phase; however, these values are qualitatively not significant. In the strip geometry, a dimensionless driving force is defined by $\Delta = u_0^2(\lambda+2\mu)/4L\gamma$. The fixed vertical displacement u_0 is applied to the strip of width L [5, 6]; $\Delta = 1$ corresponds to the Griffith point [7]. Since the phase field approach introduces a new numerical lengthscale to the problem, which is the width of the interface ξ, one has to make sure that all physical lengthscales are much larger in order to obtain results that are in quantitative agreement with the corresponding sharp interface equations. The grid can be shifted horizontally in order to always keep the crack tip in the center of the system. Thus, crack growth can be studied over long times in relatively small systems. Typical dimensions used here are 1000×500 grid points, the phase field interface width is $\xi = 5\,\Delta x$ (Δx is the lattice unit) and the Poisson ratio is $\nu = 1/3$. For the more advanced multicrack and multiphase calculations, the grids could be considerably larger (up to 8200×4100).

For being able to handle such large systems, we developed a parallel code using MPI. If we

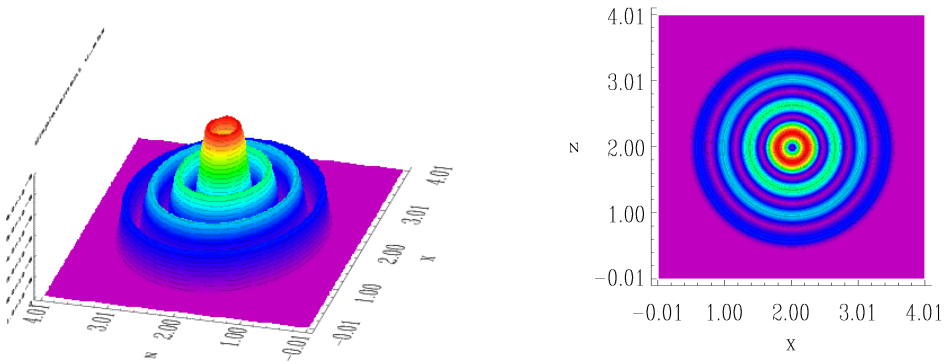

Figure 2: Isotropic emission of a sound wave by a dilatational point source. The absolute value of the displacement field $|\mathbf{u}|$ is shown color encoded and as a height profile.

increase the system size with the number of processors (weak scaling), the speedup is about 98%. In the case of strong scaling, where the same computational domain is handled by an increasing number of processors, the speedup is still an excellent 92% if we use up to 8192 cpus. The benchmark results can be seen in Fig. 1.

3 Wave propagation

First, we carefully checked the wave propagation in homogeneous media and confirmed the bulk velocities for shear, $c_s = \sqrt{E/2\rho(1+\nu)}$, and dilatational waves, $c_d = \sqrt{E(1-\nu)/\rho(1-2\nu)(1+\nu)}$. They can be determined with a precision well below 1%. From Fig. 2, one can see that the sound propagation respects isotropy.

Fig. 3 shows the amplitude of a longitudinal wave package that hits a phase boundary. The reflection coefficient R, which is defined as the ratio of the amplitudes of the reflected and the incoming wave, is given by

$$R = \frac{Z_2 - Z_1}{Z_2 + Z_1},$$

with the impedances $Z = \rho c$ for each phase. The transmission coefficient T is given by $T = 1+R$. The agreement of the numerics with theory is excellent.

4 Stress intensity factors

Close to crack tips, stresses become large, exhibiting characteristic square-root singularities which are related to stress intensity factors K, and the phase field code can also be used to extract them. For cracks with finite tip radius r_0, the stress scaling $\sigma \sim Kr^{-1/2}$ at a distance r from the tip is only valid in an intermediate regime in finite systems: Close to the tip, higher order terms can appear,

$$\sigma_{ij} = \frac{K}{(2\pi r)^{1/2}} \left(f_{ij}^{(0)} + \sum_{n=1}^{\infty} \frac{A_n f_{ij,d}^{(n)} + B_n f_{ij,s}^{(n)}}{r^n} \right), \tag{7}$$

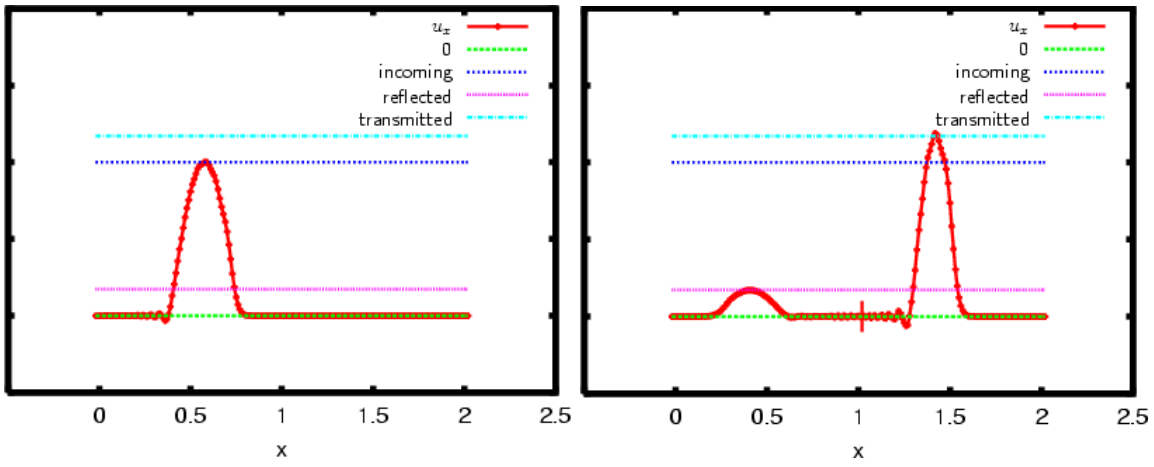

Figure 3: The left picture shows a dilatational wave package moving towards an interface which is located at $x = 1$. The picture on the right shows one part of the wave being reflected, and the remaining part transmits through the interface into a softer phase.

which are suppressed only for sharp tips. Here, the functions $f^{(n)}_{ij,d}(\theta_d, \upsilon)$ and $f^{(n)}_{ij,s}(\theta_s, \upsilon)$ are the universal angular distributions for the dilatational and shear contributions [8]. A_n and B_n are the coefficients of expansion. Far away from the tip, the stress distribution is significantly influenced by the remote boundary conditions for a finite sample. However, from the intermediate region, the stress intensity factor can be extracted. This is done here for a fast moving crack with propagation velocity $v/v_R = 0.68$ (v_R is the Rayleigh speed) subjected to a mode I loading (see Fig. 4); a deviation of about 10% for the dynamical stress intensity factor from its theoretical expectation is due to the fact that the crack opening is rather large in comparison to the system size.

5 Crack interaction and coarsening

We now also study processes with growing crack fronts or moving boundaries between phases.

The steady state growth of cracks has been carefully studied in [5], and we concentrate therefore on crack interaction here. Due to the complicated stress fields around crack tips there can be repulsive or attractive forces between them. A competition between adjacent cracks propagating in the same direction takes places because the cracks mutually reduce the effective driving force due to the elastic relaxation behind the crack tip. Therefore, for low driving forces, the cracks will attract each other and finally fuse in order to minimize the surface energy. For high driving forces, many cracks can exist and grow in the same direction, but they repel each other.

For cracks which start to grow from opposite ends of the sample, the total energy is reduced if they merge (see Figure 5).

In a large sample, many microcracks can exist, grow and merge, finally leading to complete rupture (see Figure 6). The late stage of crack coarsening processes has been studied analytically in [9]. A conventional mean field behavior [10] breaks down and multiple lengthscales become relevant in this process. Assuming a strong anisotropy which aligns the cracks perpendicular to the applied strain $u^{(0)}_{zz}$, we obtained for the evolution of the average crack length

$$R \sim \gamma k t, \tag{8}$$

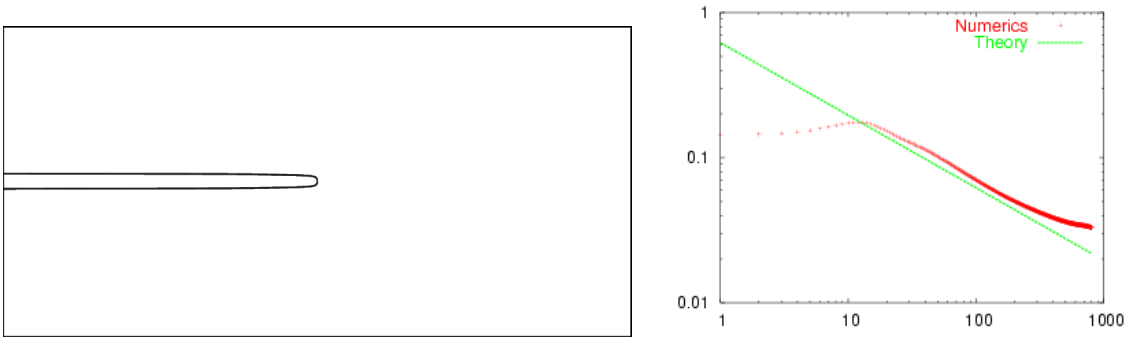

Figure 4: Determination of a dynamical stress intensity factor for the crack shown in the left panel. Right panel: The value of the vertical stress component σ_{yy} as a function of the distance from the tip is shown in a logarithmic presentation. In an intermediate regime, the square-root behavior is clearly visible.

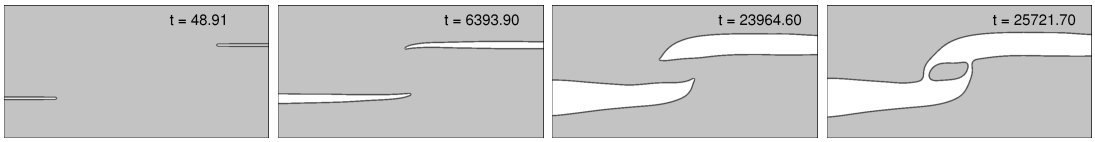

Figure 5: Two notches are cut into the sample and grow towards each other. The propagating tips cannot penetrate the already relaxed region of the opposite crack. Therefore, the cracks rest and broaden until they attract each other and fuse. We use $D/\xi v_R = 0.23$, the driving force is $\Delta = 1.8$ and the system size is 800×400 grid points. Time is given in units D/v_R^2.

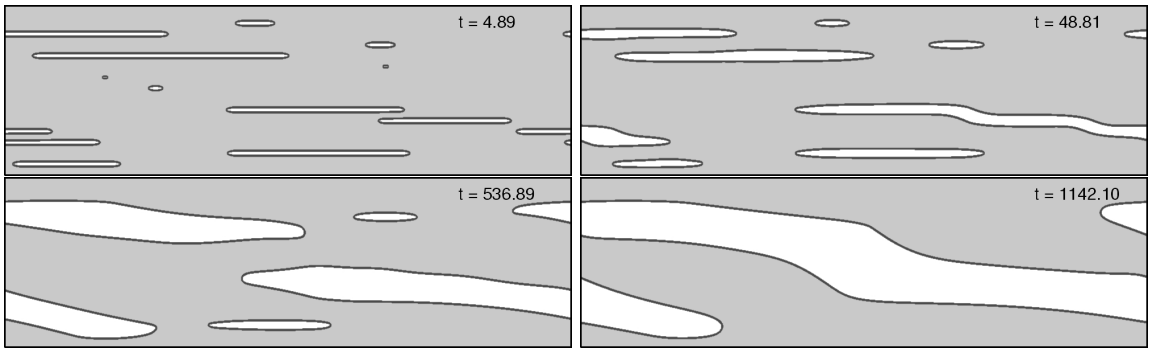

Figure 6: Coarsening of an irregular arrangement of cracks in a uniaxially strained solid with periodic boundary conditions in lateral direction. Large cracks grow at the expense of smaller cracks. The parameters used here are $\Delta = 6$, $D/\xi v_R = 2.32$, and the system size is 1000×300 grid points. Time is given in units D/v_R^2.

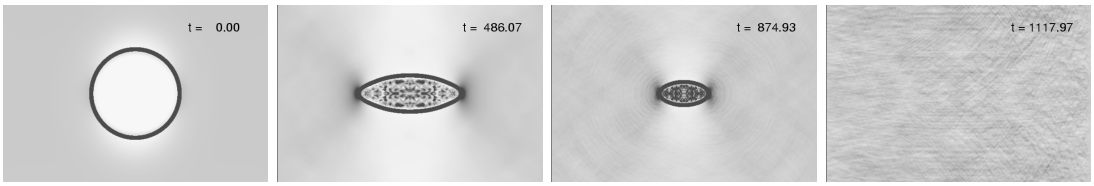

Figure 7: Shrinking of an initially spherical cavity in a uniaxially strained solid. It is energetically favorable to form an elongated inclusion, but since the applied loading is below the Griffith threshold ($\Delta = 0.9$ here) the cavity cannot grow. The gray level is proportional to the local energy density, demonstrating the propagation of elastic waves. The elastic constants of the soft inner phase are 10% of the values in the solid matrix. We use $D/\xi v_R = 1.85$, time is given in units D/v_R^2, the system size is 600×400 grid points.

with a kinetic coefficient $k \sim D$. The average vertical separation of the cracks is

$$\ell \sim \left(\frac{E}{1-\nu^2}\right)^{-1/5} \gamma \, u_{zz}^{(0)\,-2/5} (kt)^{4/5}, \tag{9}$$

and the average stress indeed decreases to zero like

$$P \sim \left(\frac{E}{1-\nu^2}\right)^{1/5} u_{zz}^{(0)\,-3/5} \, (kt)^{-4/5} \, . \tag{10}$$

Qualitatively, we see the same effect in our phase field field simulations, as neighboring cracks strongly interact with each other; in particular, the cracks avoid to penetrate the regions of material which are already elastically relaxed due to the propagation of other cracks. Obviously, longer cracks grow at the expense of shorter ones. Notice that in contrast to crack dynamics which is restricted to the tip region, cracks here can also deform behind the tip due to the phase transition model which we discuss here. In this sense, there are also strong analogies to elastically induced coarsening processes in first order phase transitions [11].

6 Elastic effects on phase transitions

Below the Griffith point cavities shrink and finally disappear. Even if they are nucleated spherically, they become oblate due to the broken symmetry of the applied elastic loading. This process is visualized in Figure 7, where the evolution of a soft droplet inside a solid matrix is shown. Sound waves, which exist in the inner phase, can hardly escape from the cavity since the transmission coefficient at the phase boundary is small. This effect is visualized by the energy density in shades of gray; darker regions correspond higher values. Notice that the interface is the only dissipative region in the system where sound waves can be absorbed. Finally, the subcritical nucleus has completely disappeared.

7 Delamination Processes

The phase field concept can also be extended to multiphase systems. Instead of a single phase field variable, we now have N fields $\phi_1, \ldots, \phi_N$ for a system consisting of N phases. They define

Figure 8: Delamination of two solid phases. The different materials are here visualized by different colors. The red and green phases are for the specific case two identical materials which are glued to each other. The initial cavity is blue.

the volume fraction of the individual phases at a certain position, and therefore they have to fulfill the conservation condition

$$\sum_{i=1}^{N} \phi_i = 1. \tag{11}$$

Again, the equations of motion can be derived from suitable functionals similar to the previous case, and material conservation (11) is obeyed by introduction of a Lagrange multiplier Λ,

$$\frac{\partial \phi_i}{\partial t} = -\frac{\tilde{D}}{\xi}\left(\frac{\delta U}{\delta \phi_i} - \Lambda\right), \tag{12}$$

with Λ being

$$\Lambda = \frac{1}{N}\sum_{i=1}^{N} \frac{\delta U}{\delta \phi_i}. \tag{13}$$

The kinetic coefficient $\tilde{D}$ now typically depends on all local values of ϕ_i and $\nabla\phi_i$ to account for different interface mobilities. This approach can also be extended to include component diffusion inside the bulk phases, see e.g. [12].

As a specific example, we demonstrate the multiphase method for a delamination process. We assume that between two layers of material a small cavity has formed as an initial interfacial crack (see Fig. 8). Since we currently do not allow for thermal fluctuations, this crack can not form spontaneously. However, nucleation processes can also be included in phase field simulations. The system is vertically loaded by a fixed displacement. For simplicity, we assume the two solid phases to be identical, but of course each phase can in principle have individual elastic properties. The "broken phase" has negligible elastic coefficients, which leads to stress free boundaries on the crack. In contrast to normal crack growth, the presence of the interlayer boundary leads to the formation of a triple junction. In full thermodynamical equilibrium, the material is completely broken and therefore all stresses have vanished. In contrast, for full lamination, the solid is homogeneously stretched and its elastic energy density is $f_{el} = \sigma_{ik}\epsilon_{ik}/2$. Complete rupture leads to an increase of the surface energy (per length of the system) by $f_s = \gamma_1 + \gamma_2 - \gamma_{12}$, where γ_1 and γ_2 are the surface energies of the solid phases and γ_{12} is the cohesive interfacial energy of the laminate. With L being the height of the sample, the condition of energy equilibrium $f_{el}L = f_s$ defines a generalized Griffith threshold for the laminate.

Above the Griffith threshold, delamination occurs, and a typical evolution of such a process is shown in Fig. 9. Here, the propagation of the crack is rather fast in comparison to the sound speed. Dissipation at the crack tips leads to the emission of sound waves which can be detected

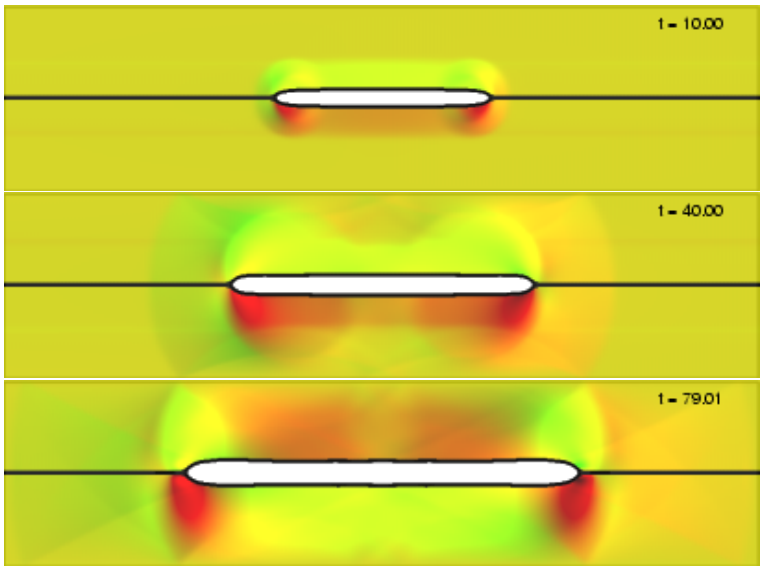

Figure 9: Delamination of two elastic strips. Time is given in units D/v_R^2 with v_R being the Rayleigh speed of the bulk phases and D the kinetic coefficient for the delamination process. The delaminated phase is shown in white. The red component for the color encoding of the elastic wave propagation is proportional to the horizontal velocity $\dot{u}_x$ and the green component proportional to the vertical velocity $\dot{u}_y$.

at the boundaries of the sample. The sound waves are visualized by color encoding.

For a nondestructive testing of the laminate the transmission of sound waves through the sample can be used (see. Fig. 10). Here, we use for example a planar dilatational wave which enters the composite from the upper boundary. When it hits the cavity, it is partially reflected and refracted, if the wavelength is not too small in comparison to the size of the crack. The emitted wave intensity is significantly reduced in regions which are shaded by the crack. Notice that for the case of equal bulk materials the waves travel without scattering through the planar boundary between them despite the presence of phase field gradients.

This work has been supported by the Deutsche Forschungsgemeinschaft under grant SPP 1120.

References

[1] L. B. Freund, *Dynamic Fracture Mechanics*, Cambridge University Press, 1998.

[2] K. Kassner et al., Phys. Rev E **63**, 036117 (2001).

[3] P. Nozières, J. Phys. I France **3**, 681 (1993).

[4] J. Virieux, Geophys. **51**, 889 (1986).

[5] R. Spatschek, et al., Phys. Rev. Lett. **96**, 015502 (2006).

[6] E. A. Brener and R. Spatschek, Phys. Rev. E **67**, 016112 (2003).

[7] A. A. Griffith, Philos. Trans. R. Soc. A, **21**, 163 (1921).

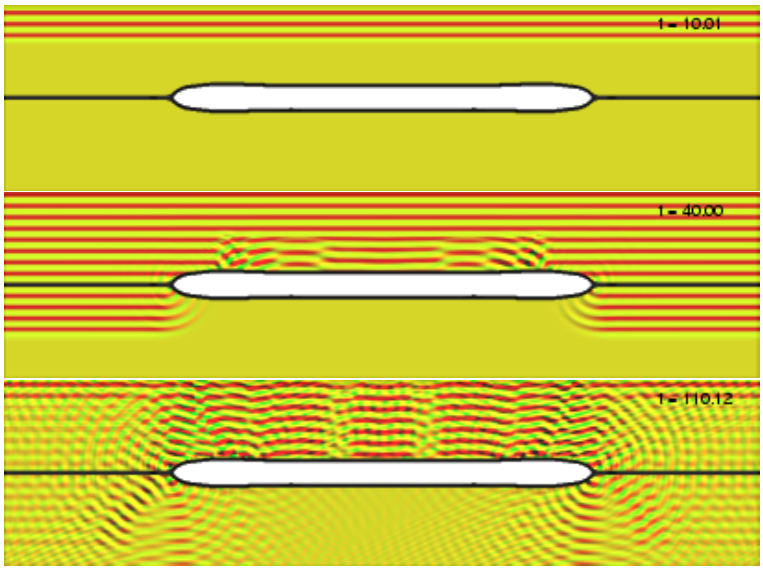

Figure 10: Scattering of a planar dilatational wave at the zone of detachment. Time is given in units D/v_R^2.

[8] J. R. Rice, Mathematical analysis in the mechanics of fracture. In Fracture: An Advanced Treatise, Liebowitz, H. Ed., vol. 2. Academic, New York, 1968, ch. 3, p. 192.

[9] E. Brener, H. Müller-Krumbhaar, and R. Spatschek, Phys. Rev. Lett. **86**, 1291 (2001).

[10] I. M. Lifshitz and Slyozov, J. Chem. Solids **19**, 35 (1961); C. Wagner, Z. Elektrochem. **65**, 581 (1961).

[11] E. Brener, V. Marchenko, H. Müller-Krumbhaar, and R. Spatschek, Phys. Rev. Lett. **84**, 4914 (2000).

[12] B. Nestler, J. Crystal Growth **204**, 224 (1999).